

# Hybrid image processing approach for autonomous crack area detection and tracking using local digital image correlation results applied to single-fiber interfacial debonding

Ilyass Tabia<sup>a</sup>, Gleb Tkachev<sup>b</sup>, Patrick Diehl<sup>a,c</sup>, Steffen Frey<sup>b</sup>, Thomas Ertl<sup>b</sup>, Daniel Therriault<sup>a</sup>, Martin Lévesque<sup>a,\*</sup>

<sup>a</sup> Laboratory for Multiscale Mechanics, Polytechnique Montreal, Canada

<sup>b</sup> Visualization Research Center of the University of Stuttgart, Germany

<sup>c</sup> Center of Computation and Technology, Louisiana State University, United States

## ARTICLE INFO

### Keywords:

Digital image correlation  
Crack surface  
Crack area  
Volume rendering

## ABSTRACT

Local digital image correlation is a popular method for accurate full field displacement measurements. However, the technique struggles at autonomously tracking emerging and propagating cracks. We proposed a hybrid approach which utilizes image processing techniques in combination with local digital image correlation to autonomously monitor cracks in a mechanically loaded specimen. Our approach can extract and track crack surfaces and provide a volume-based visualization of the crack growth. This approach was applied to single-fiber composite experimental results with interfacial debonding from the literature. Results quantitatively show that strong interfacial fiber/matrix bonding leads to slower interfacial crack growth, delays interfacial crack growth in the matrix, requires higher loadings for crack growth and shows a specific crack path distinct from the one obtained for weak interfaces. The approach was also validated against a manual approach where a domain scientist extracts a crack using a polygon extraction tool. The method can be used on any local digital image correlation results involving damage observations.

## 1. Introduction

Digital image correlation (DIC) tracks displacement fields by comparing a deformed and an undeformed image. DIC experimental setups are usually composed of a single digital image camera (2D DIC) or two cameras (stereoscopic DIC) and a mechanical loading setup. Displacements, measured in pixels, are determined by matching deformed images to a reference, or a previous image. Full displacement field measurements can then be used to compute strain fields. DIC has become a popular method for accurate full strain and displacement field measurements [1–5], to identify constitutive theories' parameters [1], and damage assessment [4,5]. Reviews by Hild et al. [6] and Pan et al. [7] provide an extensive DIC experimental mechanics applications overview. Several DIC algorithms have been developed since the 1980s, with the subset based DIC (local DIC) [8] and finite element-based DIC (FE-based global DIC) [9] being the most widely used. Global DIC algorithms usually discretize the specified Region of Interest (ROI) into elements connected by nodes, which are then traced back in the target image. All nodal displacements are thus obtained simultaneously [10]. Global DIC has strongly improved during the last decade, with some advances directly aiming at developing its ability to handle

\* Corresponding author.

E-mail address: [martin.levesque@polymtl.ca](mailto:martin.levesque@polymtl.ca) (M. Lévesque).

<https://doi.org/10.1016/j.engfracmech.2019.106485>

Received 18 November 2018; Received in revised form 11 May 2019; Accepted 20 May 2019

Available online 27 May 2019

0013-7944/ © 2019 Elsevier Ltd. All rights reserved.

discontinuities within the ROI [11,9,12].

The subset based DIC method correlates the intensity (grey levels) distribution of small pixels' subsets between a deformed and non-deformed image to determine the displacement field [13]. The subset size is defined as the set of pixels contained within a square centered on the pixel currently being tracked. The image's grey levels distribution is usually created artificially by coating the surface with random paint patterns. These patterns are usually generated by spraying aerosol paint. The subset size is conditioned by the paint dots' size since the subset should contain a recognizable pattern to yield accurate displacement fields [14]. In the subset based DIC method, each tracked pixel's displacement is obtained independently. In global DIC, displacement continuity is enforced between subsets that could be treated like finite elements with shape functions [12]. Wang et al. [9] compared the local and global DIC methods and showed that the displacement accuracy for both methods is quite similar (difference is less than 0.02 pixels). The study also showed that local DIC is more computationally efficient than global DIC. Finally, the study showed that, for subsets smaller than 11 pixels, global DIC maintains displacement robustness and might be preferred over local DIC. Another important point of this study in favor of global DIC, also highlighted by Hild et al. [12], is that global DIC can directly be compared with FEM analysis as both methods use similar discretization methods. However, thanks to its straightforward implementation, computational efficiency and accuracy, local DIC has been adopted and used in most commercial systems, making it a widely used method for experimental mechanic applications. To the best of our knowledge, global DIC has yet to be implemented into commercially available software.

When using DIC, *confidence margins*,  $C$ , are defined from a pixel's correlation equation largest covariance matrix eigenvalue [8]. A confidence of zero means that a subset in the deformed image was perfectly matched to a subset in the initial image [15].<sup>1</sup> This situation mostly occurs for purely rigid body motions. Deformed images' subsets are likely to distort and it is expected that  $C$  increases with the strain. Displacement measurements for pixels with a  $C$  above a certain threshold are usually discarded since the error is considered to be too large with respect to the corresponding non deformed subset. This pixel's tracking is therefore lost. The confidence margin's threshold is often set at values between 0.01 and 0.1 pixels [16,15,17,18]. The confidence margin's threshold is highly dependent on the standard deviation in grey levels of the speckle pattern, as well as on the average size of a feature from the speckle pattern. A confidence measurement for each pixel in its initial state can thus be determined by analyzing the speckle pattern [19]. When a discontinuity, such as a crack, appears within a speckle pattern, it drastically changes the greyscale pattern of subsets within its path and often highly deforms subsets in its vicinity. For these reasons, the  $C$  value for these subsets increases and loss of tracking ensues [15]. Smaller subsets can however reduce the area lost in the crack's vicinity, finer speckle patterns are thus sought when cracks are present [20]. With sufficiently fine speckle patterns, the area over which tracking is lost can be considered roughly similar to the crack area, as tracking loss in the crack's vicinity is quite limited [20]. Most commercial DIC software rely on subset based DIC and struggle when computing fields close to cracks. Multiscale speckle patterns are among solutions that have been introduced to perform measurements at the crack and specimen's scale during a single experiment [21,20,22]. A macro speckle pattern can thus be used to measure displacements while a finer, that is covers the same surface as the macroscopic one, can be used to either measure displacements in the crack's vicinity [20] or visualize the crack path by visualizing the areas where  $C$  is highest [21]. Such methods are applied when simultaneously tracking global and local features. Helm [23] proposed a modified local DIC implementation in which the ROI is redefined to exclude cracks, at each time step. The method requires a quasi-regular dots pattern as a speckle pattern, which produces a much more regular correlation function. Small deviations in the correlation function, meaning cracks, are thus easily detectable. However, this speckle pattern also increases possible errors during the correlation process because the texture of the subset is not sufficiently different.

Autonomous crack detection methodologies have also been developed using image processing techniques (see the review by Mohan et al. [24]). Most applications are related to crack detection in concrete materials. These techniques are limited by the crack propagation direction: i.e. crack detection when its propagation occurs in the transverse direction is less accurate than when it evolves along the longitudinal direction [25,26]. The review by Mohan et al. also showed that DIC was used in conjunctions with image processing algorithms to estimate or forecast the crack's position [27–29]. Iliopoulos et al. [27] used subset based DIC results to estimate cracks' width based on the strain field measurements. The authors found that the crack's width was overestimated due to the fact that DIC results are not sufficiently accurate close to these discontinuities. Doitrand et al. [30] estimated the size and shape of cracks at the surface of a woven composite by relying on DIC. In their work, global DIC was used with a mechanical regularization to detect cracks and their behavior. The observations were then used to predict debonding and crack densities within the composite. In 2008, Réthoré et al. [31] developed an extended global DIC algorithm with crack shape optimization. The team applied the eXtended Finite Element Method (X-FEM) methodology to measure displacements. Based on the finite element shape functions' partition of unity property, the method is able to detect straight and crooked cracks through a crack shape optimization algorithm [31,32]. The method uses Heaviside functions as an enrichment feature for global DIC nodes, allowing for a discontinuous displacement field between some of them. By relying on the X-FEM improvements to the FEM methods, X-DIC allows for measuring localized discontinuities, such as cracks. Although the method shows promising results, it relies on the global DIC framework, which is computationally less efficient and slightly less accurate than subset based DIC for subsets larger than 11 pixels [33]. Other methods, such as Acoustic Emission (AE), are required to obtain quantitative data related to the features of the crack [34]. AE uses acoustic sensors to capture mechanical waves propagating through the material due to damage events. A software can be calibrated to detect different kinds of damage events and accurate localization of damage events can be obtained by using several sensors [35].

The field of damage mechanics deals with the effects of damage on a material's mechanical response. Large international efforts

<sup>1</sup> Note that in other techniques (e.g. Electron Back Scatter Diffraction), the confidence is often best at one and worst at zero. The convention used in our manuscript follows that of VIC 3D user's manual.

are deployed to explore and understand damage mechanisms in Fiber Reinforced Composites (FRCs) [36]. Damage observations in FRCs can provide a fundamental understanding of underlying phenomena or be used to validate predictive models. The World Wide Failure Exercise (WWFE) is an international process that evaluates the predictive capabilities of a number of damage models [37]. The latest edition led to the conclusion that key experimental data is critically lacking to provide meaningful benchmark for certain loading cases and damage mechanisms [38]. More specifically, unidirectional FRCs (UDFRCs) submitted to tri-axial loadings sustain damage in the form of transverse cracks initiated through fiber/matrix interfacial debonding at a free surface [39,36]. This phenomenon was studied by Martyniuk et al. through X-ray Computed Micro-Tomography ( $\mu$ CT). Accurate interfacial crack size, growth rate and debonding angle measurements were all performed manually [39]. These types of crack measurements can serve as benchmarks to evaluate micro-mechanical damage models. Cohesive zone modeling [40] or X-FEM [41] are often used to model damage and crack growth in materials. Accurate measurements related to damage features could be used for both methods. More specifically, X-FEM enriches Finite Element (FE) shape functions in discontinuities areas and experimental data about crack growth can be used for that purpose. Moreover, the use of cohesive elements requires the a priori knowledge of the crack path, which can be obtained from experiments. Furthermore, experimental DIC results and numerical simulations correlate increasingly more as numerical simulation methods are being used to analyze DIC results, making even more relevant the availability of experimental results related to challenging issues (e.g. crack propagation). The X-DIC method enables the comparison of X-FEM results and DIC results since both methods rely on a similar description of the displacement field [11]. For example, Richefeu et al. showed how DIC results could be used to derive cohesive zone laws from full field experimental measurements of metallic alloys [42]. The method they suggested consisted firstly in identifying the zone through which a mode I crack grew, from DIC measurements. Then, they applied a micro-mechanical damage model to consider damage through isotropic straining of the specimen's cross section, and estimated a local stress-strain profile from which a cohesive law was derived.

This paper presents a hybrid approach where local texture features derived from camera images via image processing are combined with commercial DIC confidence software data to autonomously identify crack areas. This approach consists in using the DIC confidence results as a filter to determine possible areas where a crack grows. The exact crack shape is then obtained by combining image processing algorithms, a set of morphological operations and an entropy function. The crack can be detected independently of its shape, or growth path, and this work is performed at a very small computational cost thanks to the DIC results that restricts the image processing algorithm search areas.

We have applied our algorithm to study crack propagation in a single-fiber composite where the fiber was submitted to a transverse load. The experimental data used in this work was obtained by Tabiaï et al. [43] and consists of local DIC measurements in the fiber's vicinity while damage is growing around it.

Section 2 recalls the experimental setup for both experiments analyzed in this work. Section 3 provides background information on DIC's limitations with respect to crack monitoring. Image processing techniques used in the hybrid method are addressed in Section 3.2. The hybrid approach and its application are exemplified with a single DIC image involving damage in Section 4. The crack path visualization in the reference frame, the crack area growth and the volume-based rendering for both specimens analyzed using the hybrid method are presented in Section 5. The parameters used and their impact on crack extraction's accuracy are studied in Section 6. Finally, Section 7 concludes this work and presents outlooks.

## 2. Experimental methods

### 2.1. Experimental setup

The experimental data presented herein was obtained from [43]. The complete raw experimental data is available on Zenodo and can be obtained for further analysis [44].

#### 2.1.1. Specimens

The specimens analyzed in this work were composites containing a single-fiber embedded into a standard dog bone specimen and aligned through its thickness. The specimen's configuration is presented in Fig. 1.

The matrix was a thermoset epoxy having a Young's modulus of 2.5 GPa and a Poisson's ratio of 0.44 [43]. Two different materials were used as the fiber [43]: a 0.90 mm galvanized steel wire and a 0.99 mm Polytetrafluoroethylene (PTFE) monofiber. PTFE is a non-reactive synthetic polymer with a very low coefficient of friction (0.020–0.2 according to the manufacturer) [45] and its reported surface energy is not sufficiently high to bond with epoxy [46]. Thus, a PTFE fiber inside an epoxy matrix can only be held through compressive residual forces generated after manufacturing due to the difference in coefficients of thermal expansion (CTE) between the matrix and fibers. Galvanized steel fibers were chosen for their high bonding strength with epoxy [47]. The coefficient of friction of the galvanized steel is estimated to be about 0.31 [48]. These two different fiber/matrix couples are expected to exhibit different damage evolution that can be quantitatively evaluated by analyzing damage features.

#### 2.1.2. Tensile test setup

Each specimen was setup in an *Insight* MTS electromechanical testing frame mounted with a 25 kN loadcell. A three-axis precision stage carrying a *VIC-3D™* stereo-microscope system (acquired from *Correlated Solutions Inc*) was placed in front of the tensile testing machine to acquire stereo images. Fig. 1 schematically shows the observed specimen area.

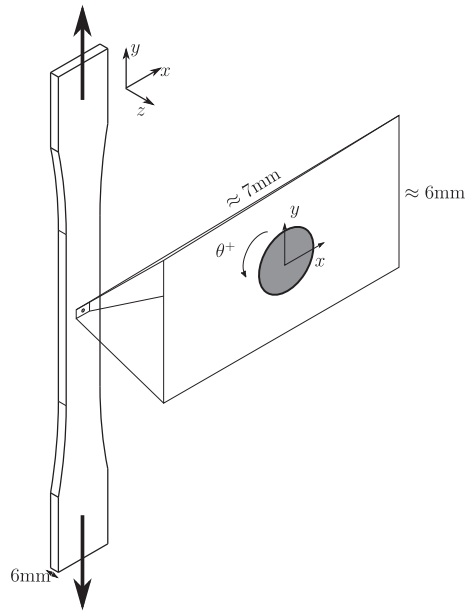


**Fig. 1.** Tensile test specimen used. The arrows show the tensile direction. The fiber is visible as a circle in the middle of the specimen. The cameras observe the specimen in the  $xy$  plane in an area of  $7\text{ mm} \times 6\text{ mm}$ .

## 2.2. Displacement field measurement by local subset based DIC

### 2.2.1. Speckle pattern

A thin layer of white acrylic spray paint (*Ultra 2X spray paint, Painter's Touch*®) was applied on the specimens' polished side. A mist of black paint was then applied on the white layer to produce a suitable speckle pattern.

The speckle pattern's quality was assessed with the commercial software *VicSnap* (DIC version 8-b245, acquired from *Correlated Solutions Inc*). The software compares the displacement field obtained by DIC for an artificially deformed image for which the imposed deformation is known [8]. The speckle pattern was modified by changing the average dot size and their distribution until the smallest possible confidence margins for the Region of Interest (ROI) was reached. The pattern was improved by removing the paint and re-applying it on the specimen. A  $C$  threshold of 0.050 pixels was chosen. Any pixel for which  $C$  was higher than 0.050 pixels was discarded. An optimized 8-tap interpolation scheme was used for sub-pixel interpolation. *VIC3D* uses an affine subset shape function [49,15]. Lagrangian strains were computed using a decay filter of 5 pixels to minimize smoothing of the raw experimental data while computing strains.

### 2.2.2. DIC software parameters

The DIC algorithm provided by the commercial package *VIC3D* [15] relies on two main parameters:

**Subset size.** A large subset would not be adequate to capture strain gradients around small geometrical features, such as the fiber [15]. A subset as small as possible was therefore sought.

**Step size.** The step size is defined as the spacing between analyzed pixels. A step of 2 means that one pixel out of two is tracked. The other pixel's displacement is interpolated [15].

**Spatial calibration.** The stereo-microscope was adjusted and calibrated for distortion, in-plane and out-of-plane displacement measurements, before each test [8,15]. The detailed calibration results were provided with the complete dataset of the experiments analyzed in this work [44].

The displacement spatial resolution measurement represents the distance between two completely independent displacement measurements. Subsets are used to measure a single pixel's displacement, thus the distance between two independent measurements is a subset size [50,8]. Since the step was set to 2 and Lagrangian strains were computed using a 5 pixels decay filter, the total smoothing area due to strain computations was of 10 pixels. The strains' spatial resolution, also called the effective strain gauge length, represents the distance between two completely independent strain measurements and was computed as per:  $\text{Step} \times (\text{Strain Filter}-1) + \text{Subset}$  [8]. The effective strain gauge length was computed to be of 648 pixels for the PTFE/epoxy specimen, and 680 pixels for the galvanized steel/epoxy specimen.

The current study is focused on analyzing a crack initiation and growth from DIC results. High strain gradients are expected in the vicinity of the crack area. Smoothing of full field measurements would hide the high strain gradients. For these reasons, a subset as small as possible was sought by trying to obtain the finest speckle pattern possible. A step of two was deemed an acceptable compromise between computational time and smoothing through interpolation.

The three-axis precision stage was used to move the stereo-microscope image acquisition setup to keep the fiber in the cameras'

**Table 1**

Subset and step parameters selected for each analysis.

Matrix	Fiber	Subset	Step	Correlation
Epoxy	PTFE	81	2	Direct
Epoxy	Galvanized steel	85	2	Direct

frame while the specimen was mechanically loaded. It was firstly immobilized against the tensile testing machine. Dampeners were used under the three-axis precision stage to avoid any movement and minimize vibrations. The three-axis precision stage's positions was manually adjusted with precision rails. A stereovision system was chosen to measure all components of displacement without introducing full-field measurement errors, even though the ROI may undergo out-of-plane translation and rotation. Table 1 lists the main DIC parameters (subset, step and correlation types) used for each test.

### 3. Background

#### 3.1. Damage and crack tracking with DIC limitations

Fig. 2 schematically shows how pixels about half a subset size away from the ROI's edge and those in crack's vicinity cannot be tracked. Fig. 2a shows that pixels must be surrounded by a subset so that the speckle within its initial subset can be recognized. Subsets on the ROI's edge do not have enough pixels surrounding them to be tracked. Fig. 2b shows a crack in black growing through the ROI and how it affects subsets in its surrounding. The confidence  $C$  for subsets located in the crack's surroundings increase with its growth, which induces loss of tracking. Moreover, tracking is usually lost around a crack due to the large strains encountered in this area, even if the speckle pattern is unaltered. Crack tracking based solely on  $C$  delivers crack areas over-estimations.

Moreover, tracking is usually lost around a crack due to the large strains encountered in this area, even if the speckle pattern is unaltered. Crack tracking based solely on  $C$  delivers crack areas over-estimations.

Through the application of image processing methods and combined with a 3D spatial calibration, stereo-DIC provides displacement measurements. However, these measurements are limited and do not provide the crack's features themselves. Additional image processing technique, combining new information extracted from the raw images and the subset based digital image

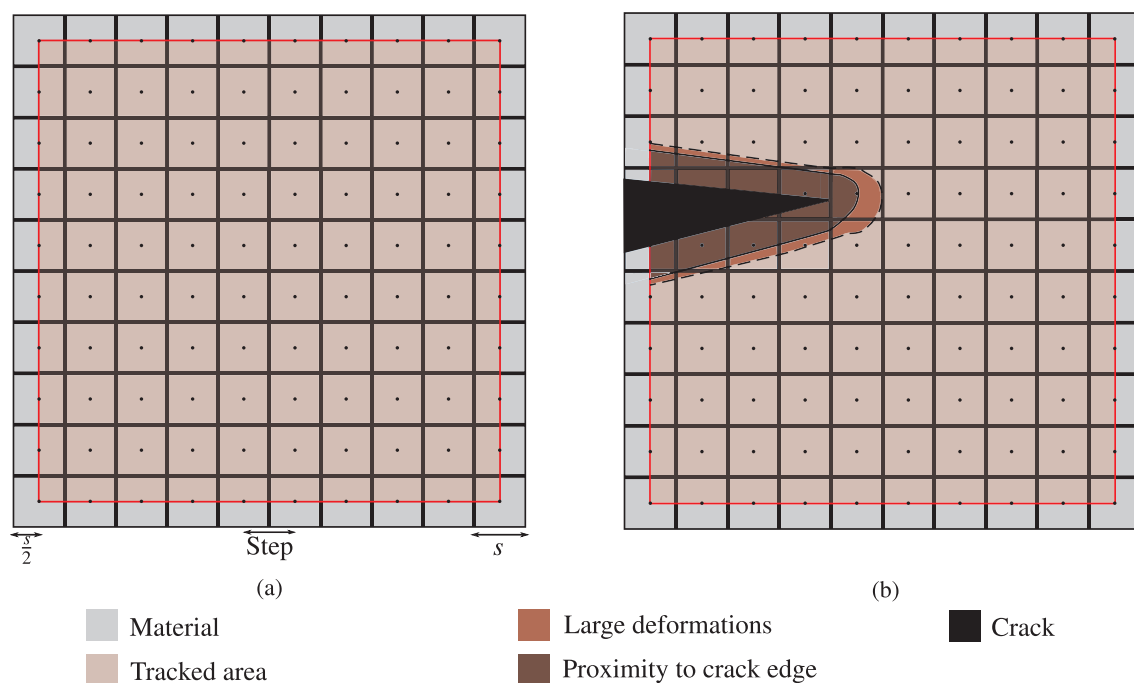


**Fig. 2.** Schematization of the influence of the crack on DIC accuracy. (a) Represents an undeformed surface under observation. The large gray square represents the surface that was covered with a speckle pattern. The grid drawn is used to represent the subset size. The black dot at each subsets' center represents the tracked pixel. Since a whole subset is necessary to track a single pixel, the interpolation area is delimited by the red rectangle. (b) Represents the same surface once a crack (represented here in black) grew within the material. Subsets for which the speckle pattern is modified by the crack are represented in dark brown. These subsets can no longer be tracked because the speckle pattern has significantly been modified. Areas covered in red, all around the dark brown areas for which tracking is lost, represent areas for which  $C$  becomes higher due to significant deformation. (For interpretation of the references to color in this figure legend, the reader is referred to the web version of this article.)

correlation methods are here proposed to measure the crack's feature.

### 3.2. Image processing methodology

Morphological operations [51] transform a binary image (*i.e.*, and image of zeroes and ones) by applying operators to every pixel and its neighbors. A pixel's neighbors are defined by a so-called structuring element, which is itself a small (*e.g.*,  $3 \times 3$ ) binary image centered around the target pixel.

The two most basic morphological operations are dilation and erosion. Dilation assigns each pixel the maximum value among its neighbors (including itself), which for the case of a binary image means assigning 'one' if and only if there is at least one non-zero pixel among the neighbors. This effectively expands continuous regions of 'ones' outwards. Erosion is the opposite operation using the minimum instead of the maximum, thus shrinking the 'one' regions.

Dilation and erosion operations define the morphological scale space. Applying sequences of dilations or erosions results in expanding or shrinking the shapes in the image, corresponding to moving up or down in the scale space. This can be helpful in removing noise. For example, a series of erosions helps separating small weakly connected regions of 'one' from larger regions.

Morphological thinning [52], also called skeletonization, is based on the hit-or-miss transformation that considers small subsets around each pixel and compares them to some predefined template. The operation sets to 'one' only the pixels whose neighbors match the structuring element. Morphological skeletonization can be performed by continuously applying thinning, thus reducing the binary image to one-pixel-wide skeletons that capture the original image's topology. Morphological pruning [53] defines the structuring elements such that the ends of thin line segments are removed. Pruning is useful for post-processing the skeleton by removing small branches that do not significantly contribute to its overall shape.

The discrete entropy  $H$ [54] is defined as:

$$H(\mathbf{X}) = - \sum_{i=1}^n P(x_i) \log_2 P(x_i), \quad (1)$$

where  $X$  is a discrete random variable with  $n$  possible values  $\mathbf{X} = x_1, x_2, \dots, x_n$  and  $X$  a probability mass function  $P(x)$ . The entropy can be used as a measurement of the distribution's uniformity. In our case,  $H(\mathbf{X})$  was computed for pixel values in a small image subset to estimate the image's local heterogeneity. This estimate was maximized when all pixel values were uniformly distributed (*e.g.*, white noise), and was minimized when all pixels had the same value.

All image processing operations were implemented in Python using SciPy [55] (entropy) and Scikit-Image [56] (image histograms, morphology) packages.

## 4. Crack area extraction in single fiber composites with DIC and image processing alone

The techniques presented in Section 3.2 were applied to an arbitrary image containing a crack acquired during a tensile test on the PTFE/epoxy specimen. Fig. 3 shows snapshots for the PTFE/Epoxy specimen (a) before damage, (b) at the onset of damage, and (c) at the onset of crack kinking. Each pixel corresponds to approximately  $3.1 \mu\text{m}$ . Fig. 3 also shows the confidence margins  $C \in [0, 1]$  for the displacements provided by VIC-3D™ [15] as a contour plot in the second row. Fig. 3d shows that the confidence value close to the fiber-matrix interface increases even for small loads, which means that significant deformation occurred in those areas. Fig. 3e and f show that  $C$  increased in other areas as the load increased. It is possible to notice that the stress applied on the specimen decreases after Fig. 3b due to the growth of the interfacial crack.

The chosen image is shown in Fig. 4a and is used throughout Section 3.2 to exemplify DIC-based and image processing-based crack extraction algorithms' limitations on our specific experiment.

### 4.1. DIC-based crack extraction

The DIC-based technique assumed that the pixels belonging to the crack are those for which correlation was lost.

A binary image was constructed first by encoding pixels with a match as 'zero' and the unmatched pixels as 'one' (white pixels in Fig. 4b). Besides the main unmatched area around the crack, the image also contains thin lines of unmatched pixels. These lines result from two neighboring pixels in the reference frame being tracked to the same pixel in the target frame, leaving a nearby unmatched pixel in the target frame. We convolved the image with a Gaussian kernel that removed high-frequency details from the image, effectively blurring it, to remove the untracked pixels. We then thresholded the resulting image, marking as 'one' all pixels with value above 0.5. The overall operation fills in unmatched pixels that are surrounded by mostly matched pixels and produces a locally coherent image without the noise (Fig. 4c). The image's left and right border exhibit unmatched pixels that result from the fact that the ROI moved away from the camera's frame during the test. These areas can be manually removed by ignoring the regions of unmatched pixels immediately adjacent to the ROI's borders.

The next step consisted in removing noise in the binarized image. This was achieved by performing a set of morphological operations. Fig. 5 presents an overview of the operations used.

All continuous regions having a total area below a threshold were removed. This operation removes holes and objects (*i.e.*, small continuous regions of 'zeroes' and 'ones', respectively). Then, filtering was performed at a different morphological scale (Section 3.2). A sequence of erosions was applied, followed by removing small disconnected objects. A complementary sequence of dilations was



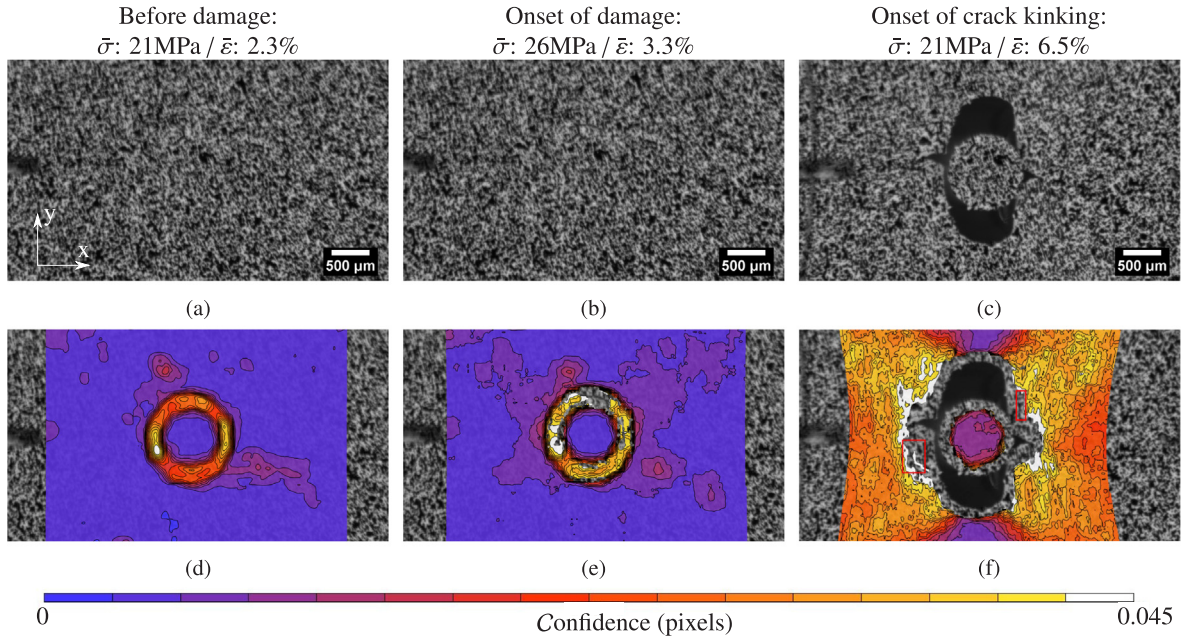


**Fig. 3.** PTFE fiber/epoxy composite loaded in tension in the  $y$  direction: (a) before damage, (b) at the onset of visually distinguishable damage, and (c) at the onset of crack kinking. The first row shows raw images taken by the camera and the second row the corresponding confidence margins  $C$  provided by the DIC software. The red rectangles in image (f) show pixels for which tracking was lost due to the large strains present in this area.  $\bar{\sigma}$  is the nominal stress applied by the machine on the specimen and  $\bar{\epsilon}$  is the nominal strain applied on the specimen and was computed by dividing the crosshead's displacement over the specimen's ungripped length. (For interpretation of the references to color in this figure legend, the reader is referred to the web version of this article.)

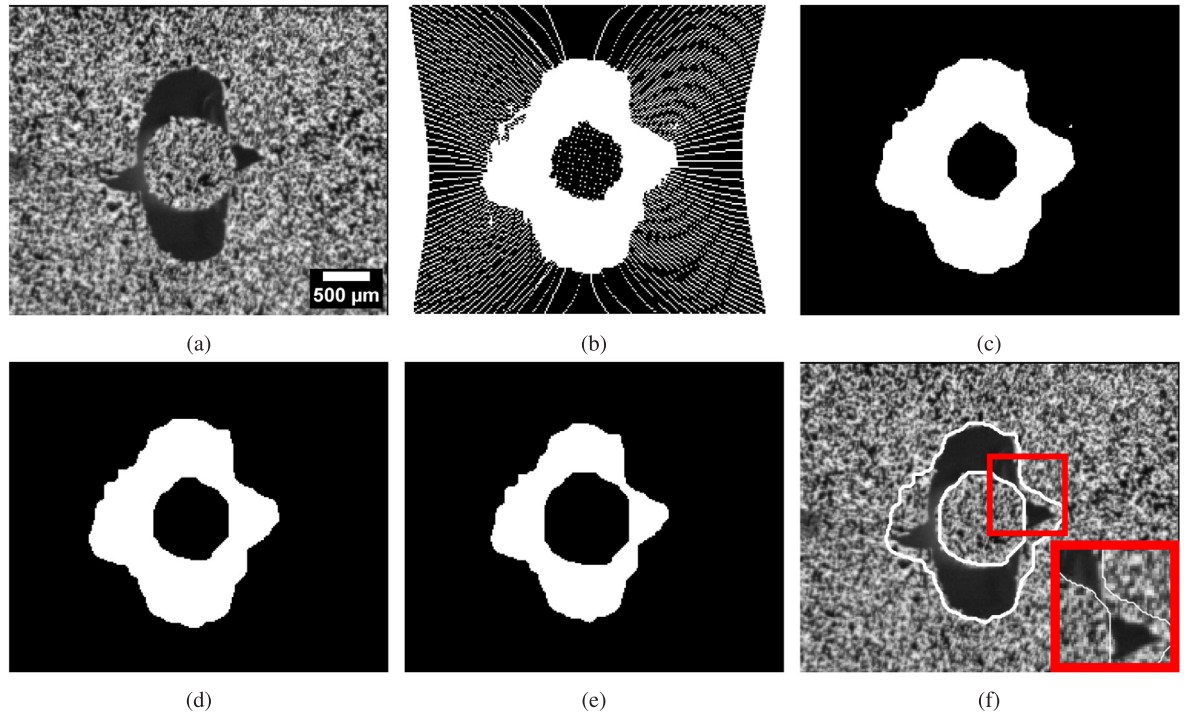


**Fig. 4.** Crack extraction using DIC tracking data for the PTFE/epoxy specimen with  $\bar{\sigma} = 20.2$  MPa and  $\bar{\epsilon} = 6.7\%$ : (a) Original camera image. (b) Pixels in the target frame that were not matched from the reference frame are encoded as white. (c) Unmatched pixels after a Gaussian filter and thresholding. (d) Image obtained after morphological filtering: small holes and objects are removed. (e) Final image after erosion, compensating for the DIC subset size. (f) Contour of the final image overlaid over the original camera image. The DIC-based method provides only a rough crack shape estimate and overestimates its area.

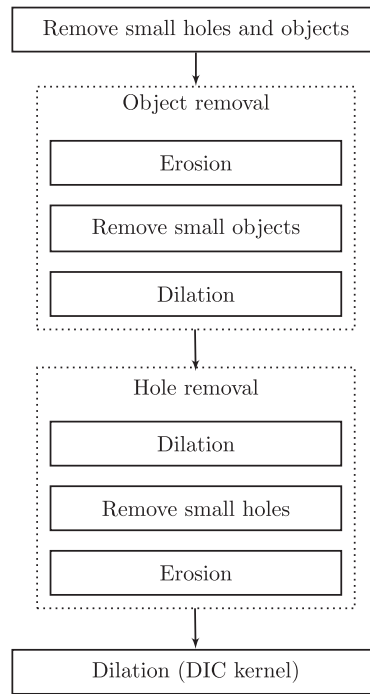


**Fig. 5.** An overview of the filtering performed on the unmatched pixels, which were extracted from the tracking data. The filtering was achieved by using morphological operations: objects with small area were removed between erosion and complementary dilation. Holes were removed in the opposite sequence: dilation first, holes with small area, and erosion back.

performed to return back in morphological scale space. The operation was repeated next, but in the opposite direction: applying a sequence of dilations, removing small holes and applying a complementary sequence of erosions. The result is presented in Fig. 4d.

The resulting crack area requires compensation for the subset size used for DIC. The need for this compensation is illustrated in Fig. 2b, where pixels lost tracking not only when they were directly in the crack area, but also when the crack was nearby, strongly deforming the material in this vicinity. As a result, the area that lost correlation is larger than the actual crack. Another sequence of erosions was applied, with the number of erosions equal to DIC subset's the half-size, to compensate. The final image represents the estimated crack area (Fig. 4e, f). The crack area obtained using DIC-based extraction method overestimates the visible crack area.

#### 4.1.1. Image-based extraction

Our image-based method relies on the visual disparity between the crack and the speckle pattern painted on the specimen. Specifically, it was assumed that the crack areas were roughly homogeneous and that the speckle pattern exhibited a high variance. For this reason, an entropy filter that computes local entropy was applied around each pixel, with a subset size of 9, which is 0.8 time the DIC subset size. The result is shown in Fig. 6a. It was then binarized with a threshold of 1.0 natural units (studied in Section 6.3). Fig. 6b shows the binary image. A sequence of dilations, the number of which was equal to the subset's half-size, was then performed to compensate for the filter subset size to obtain the final result (Fig. 6c and d).

This image-based method relied on a subset (neighborhood) around a pixel for computation, thus making the subset size an important parameter with a significant effect on the result (similar to how DIC subset size affects the tracking results). If we use a



**Fig. 6.** Crack extraction using texture features in the original camera images for the PTFE/epoxy specimen with  $\sigma = 20.2$  MPa and  $\epsilon = 6.7\%$ . (a) Local entropy of the camera image. (b) Local entropy after thresholding into a binary image. (c) Final image after compensating for the local entropy subset size. (d) Contour of the final image overlayed over the original camera image. The image based method appears to underestimates the crack area.



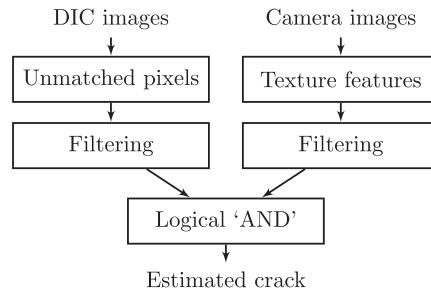


**Fig. 7.** An overview of our proposed crack estimation approach. First, the DIC tracking data is used to determine which pixels were not matched from the reference frame. This produces a rough crack shape. Texture features are extracted from the camera image and filtered to obtain an image-based result to refine the DIC crack estimate. Finally, the two images are combined together to obtain a more accurate crack area through a ‘AND’ boolean operation.

smaller subset, the method detected the shape of the crack boundary more accurately, but became less robust and produced false-positive results, confusing small cracks and the speckle pattern. A false-positive mistakes an area of the image which is not a crack for a crack. For this reason we opted to combine our image-based and DIC-based methods into a hybrid approach described in Section 4.2.1.

## 4.2. Crack area extraction with the hybrid method

### 4.2.1. Hybrid crack extraction

Our hybrid crack extraction method which combines DIC-based and image-based analysis is depicted in Fig. 7. Specifically, image-based crack detection was restricted to the areas near our DIC-based crack identification, which allowed for computing local entropy with a reduced subset size. This results in a more accurate crack shape, while the restricted search area filters out potential false-positive results.

First, we took the DIC-based crack area obtained in Section 4.1 and applied a sequence of three dilations to expand our search area. The result is shown in Fig. 8a. Then, an image-based crack area is computed using a smaller subset size of 5, which is  $0.4 \times$  DIC subset size (Fig. 8b, cf. Fig. 6b), followed by the compensation for texture filter subset size (similarly to Section 4.1.1). Finally, a logical ‘AND’ operation was performed: a pixel belongs to the crack if both the image-based and the dilated DIC-based methods classified it as a crack to obtain the final crack estimate in Fig. 8c, d. It is better to apply the compensation after combining the results, otherwise dilation would also apply to any false-positives caused by a small subset size. Note, that this hybrid method achieved better accuracy than both the pure image-based and the DIC-based solutions, while still avoiding false-positive results.

### 4.2.2. Crack path in the reference frame

The crack path computation was based on the DIC confidence values  $C$  in the reference frame (as opposed to the crack area extraction, which was performed in the target frame). First, the confidence values for each pixel of the frame were thresholded to obtain a binary image where the lost pixels are encoded as ‘ones’. Fig. 9a shows the binary image obtained after thresholding confidence values. A sequence of binary erosions was performed, followed by removing small disconnected regions of ‘zeros’ to remove small noise resulting from tracking errors (Fig. 9b). Next, the crack topology was obtained by extracting its skeleton through continuous morphological thinning, which reduced continuous regions to one pixel. The obtained path was then further filtered with morphological pruning. The resulting topology is shown in Fig. 9c. Some small irregularities in the shape were still observed, but overall a crack path estimation in the reference frame in accordance with the one in the deformed frame was obtained.



**Fig. 8.** Crack extraction using the hybrid method for the PTFE/epoxy specimen with  $\sigma = 20.2$  MPa and  $\epsilon = 7\%$ . (a) DIC-based crack estimate after a round of dilations. (b) Image-based crack estimate using a smaller subset size. Note the false-positive regions produced by imperfections in the speckle pattern. (c) Final image after combining the DIC- and image-based estimates, compensated for the entropy kernel size. (d) Contour of the final result overlaid over the original camera image. The hybrid method appears to produce an accurate crack area estimate.

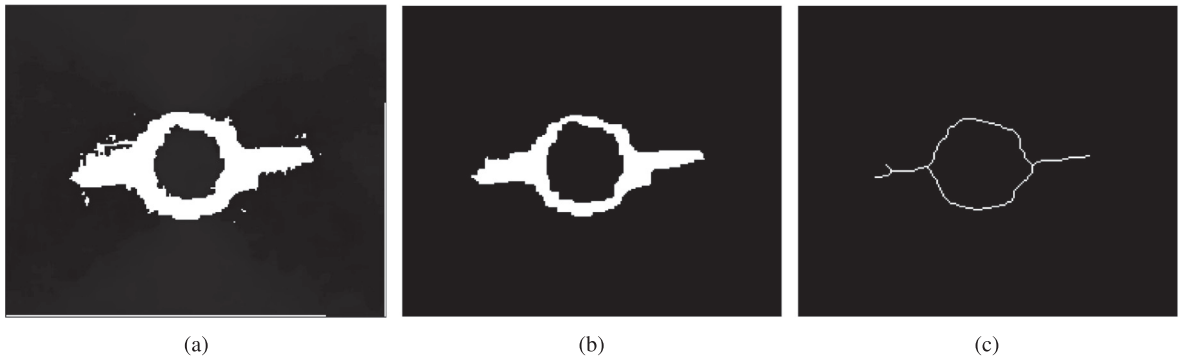


**Fig. 9.** Crack path extraction in the reference frame for the PTFE/epoxy specimen with  $\bar{\sigma} = 20.2$  MPa and  $\bar{\epsilon} = 6.7\%$ . (a) Thresholded confidence values  $C$ . White represents pixels in the reference frame that lost correlation. (b) Results after morphological filtering. (c) Final crack path estimate obtained through morphological skeletonization.

## 5. Application of the hybrid method to the experimental data set

### 5.1. Crack path visualization in reference frame

**Fig. 10** compares the extracted crack area in the target frame (top row) and crack path in the reference frame (bottom row) for the PTFE/epoxy specimen after interfacial debonding propagated around the fiber. The images are presented in a chronological order, from left-to-right. The first column corresponds to one of the experiment's earliest frames. While it is possible to see the first crack areas, it is not yet possible to reliably detect them due to their small size with respect to image's resolution (**Fig. 10a**). Reducing our image-based method neighborhood size (described in Section 3.2) could help, but would also introduce false-positive results. However, we can already see the forming crack path in the reference frame (**Fig. 10e**). It is possible to notice that the crack path in the reference frame is slightly longer than the apparent crack. Crack path extraction is solely based on the DIC data, and some pixels already start to loose tracking. Areas in the crack's vicinity are subjected to large deformation and thus have large confidence values, thus the area at the tip of the crack is often considered as being part of the crack tip. In the second column, we see one of the earliest frames with a detectable crack area (**Fig. 10b**). At this point in time, the crack path in the reference frame is fully formed around the fiber (**Fig. 10f**). The third column demonstrates the stage at which the crack starts spreading horizontally. We are able to accurately extract the crack area, as well as detect its horizontal propagation (**Fig. 10c, g**). The last column shows the crack area detected on the

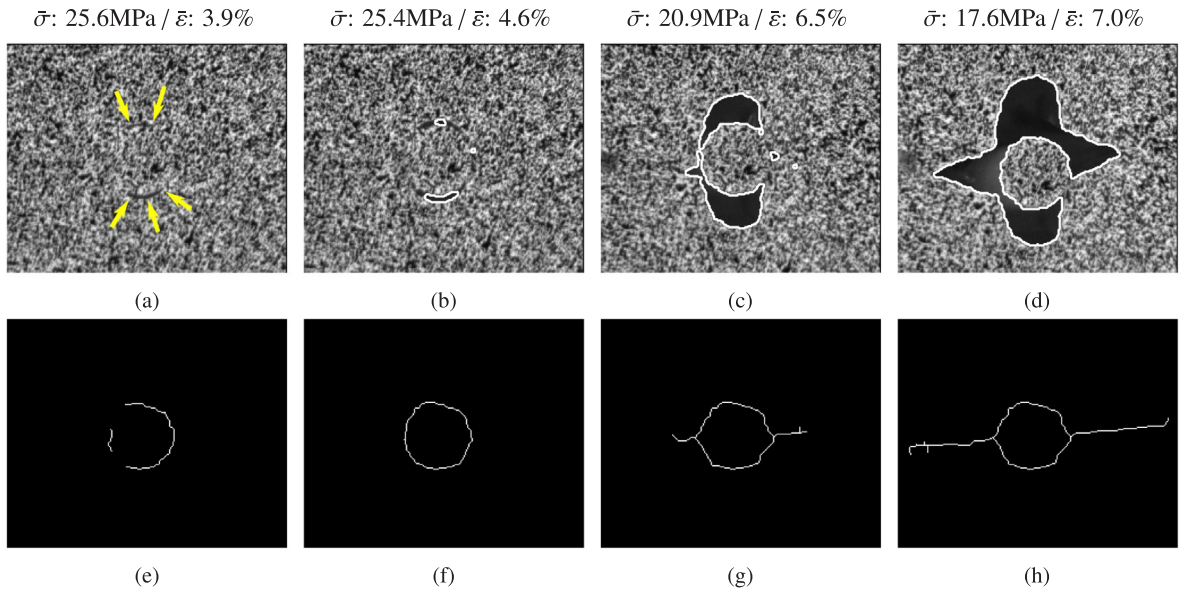
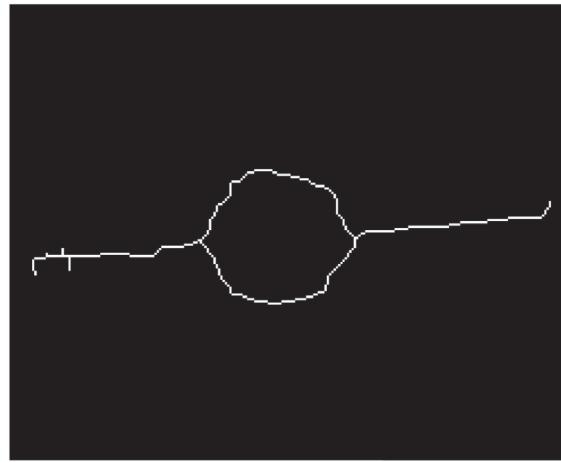
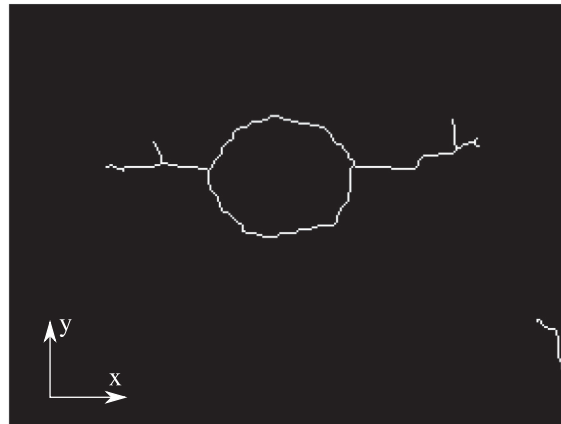


**Fig. 10.** Timelapse of the crack area detection and extraction presented for the PTFE/epoxy specimen. Top row: results of the hybrid crack area extraction in the target frame. Bottom row: result of crack path extraction in the reference frame. Images are arranged chronologically, left-to-right. First column: early in the experiment the first visible cracks appear. Second column: first extracted cracks. Third column: crack starts to propagate horizontally. Fourth column: later stages of the experiment. Yellow arrows were added in the first image of the first row to emphasize the position of the initial crack. (For interpretation of the references to color in this figure legend, the reader is referred to the web version of this article.)



(a) PTFE fiber with epoxy matrix at a global strain level of 7% and global applied stress of 17.5 MPa



(b) Galvanized steel fiber with epoxy matrix at a global strain level of 8.8% and global applied stress of 17.7 MPa

**Fig. 11.** Crack path extraction for two different sets of fiber/matrix. The crack path in the reference frame shows how the fracture pattern is affected for different materials. Both cracks are represented using the same scale.

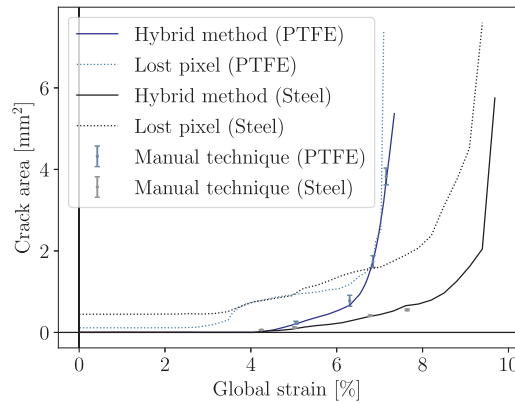
picture and crack path in the reference frame detected before specimen failure (Fig. 10d, h).

Fig. 11 shows the crack path extracted for the PTFE/epoxy and galvanized steel/epoxy specimens. Without any bonding, the interfacial crack grows in a symmetrical manner for the PTFE/epoxy specimen, at about the same rate for the crack visible above and below the fiber. This reveals a transverse crack path perpendicular to the applied load direction that crosses the fiber's diameter, as shown in Fig. 11a. For the galvanized steel/epoxy specimen, interfacial crack growth does not happen at the same rate for the crack above and the one under the fiber. This might be attributed to the fact that the interfacial bonding strength might vary around the fiber. Although the crack path is perpendicular to the applied load direction, it is offset in the positive  $y$  direction, as shown in Fig. 11b.

#### 5.1.1.1. Crack area growth

Fig. 12 shows, as continuous lines, the crack area determined using our hybrid method. The crack area obtained using the hybrid method for the PTFE/epoxy specimens is plotted in blue, while that for the galvanized steel/epoxy is plotted in black. The crack area was also manually measured using a polygon selection tool from an image processing software to validate the obtained results (from the open source *ImageJ* software) at four different time-steps, for each specimen. Since crack extraction remains an error-prone task, even for a domain expert, each measurement has been repeated five times. Fig. 12 reports the average crack area value manually measured for each time-step as well as their 95% confidence intervals. The manual and hybrid results are reasonably consistent with a maximum error for the hybrid method with respect to the manual measurements of 12%. This error is high at the beginning of the experiment because the crack area is still small, thus, small variations have a relatively higher impact on the method's relative accuracy.

The crack size area estimated from the lost pixels is also reported in Fig. 12. This crack size estimate obtained using the DIC data



**Fig. 12.** Estimated crack area as a function of the applied strain. The area obtained for the PTFE/epoxy and galvanized steel/epoxy specimens are shown as blue and black lines, respectively. Four manual crack size measurements (using the *Polygon selection tool* from the open source *ImageJ 1.51* software) were performed by a domain scientist at arbitrary moments during the test to compare results with the measurements performed using the hybrid method for each specimen. Each manual measurement was performed five times, the average for each measurement is shown as a cross and the standard deviation is represented as an error bar. An estimate of the crack area using the sum of areas covered by pixels for which tracking was lost is also shown as a dotted line. It is possible to see how the estimate obtained from DIC overestimates the real crack area, while the hybrid method and human measurements provide the same results.

overestimates the real crack size. The manual and hybrid method measurements provide the same results and are consistent.

Fig. 12 shows that the cracks in both the PTFE/epoxy and galvanized steel/epoxy specimens started growing at around the same moment, slightly after an applied global strain of 4%. The plot shows that crack initiation appears to be independent of the fiber/matrix bonding strength, as it occurs at the same applied global strain for both specimens. The PTFE/epoxy specimen's crack then grows linearly up to 6.5%. The galvanized steel/epoxy specimen's crack also grows linearly but at a slower rate than that in PTFE/epoxy specimen. This observation might be due to the stronger bonding between epoxy and galvanized steel/epoxy. A significant increase in the crack growth rate for the PTFE/epoxy specimen can be noticed for a global strain of about 6.5%. This increase is due to the interfacial crack growth in the matrix, as shown in Fig. 10c. The crack then keeps growing until specimen failure is reached for a global strain of about 7.2%. Interfacial crack growth in the matrix for the galvanized steel/epoxy specimen appears to be delayed as it only happens for a global strain of about 9.5%. This suggests that the strong bonding between galvanized steel and epoxy slows the crack growth rate down, which is not the case for the PTFE/epoxy specimen. Interfacial crack initiation thus appears to be independent of the fiber/matrix bonding properties under transverse load. However, crack growth within the matrix strongly depends on the fiber/matrix bonding properties.

## 5.2. Volume-based rendering of time-dependent crack growth

A volume visualization was produced by stacking extracted two-dimensional crack regions chronologically, along the third dimension. It provides a concise crack growth overview and is presented in Fig. 13.

Additionally, the crack regions were colored according to the global strain level at which tracking was lost for the pixel.

This volume representation allows to rapidly observe that, for the galvanized steel/epoxy specimen (Fig. 13b), the crack originates above the fiber first, then initiates under it while still growing at the top. The crack remained localized at the fiber's top and bottom areas. For the PTFE/epoxy specimen (Fig. 13b), the crack initiated almost simultaneously at its top and bottom areas, and then grew all around it while symmetrically growing in the matrix time in the transverse direction, at a roughly uniform rate. These images directly show that the galvanized steel/epoxy specimen offered more resistance to crack initiation and growth than the PTFE/epoxy specimen did.

## 6. Discussion

### 6.1. Tracking loss due to large deformation

At the beginning of each test, the specimen is undamaged and no areas are subjected to large deformation yet. There should thus be no pixels for which tracking is lost. As shown in Fig. 12, this is true for the PTFE/epoxy specimen only. Analysis of the complete experimental results presented in [44] shows that, due to the quality of the speckle pattern, pixel tracking was lost from the very beginning of the test for a few pixels. Fig. 12 also shows that crack growth becomes significant higher after a global applied strain of 4%. It can however be observed that, between an applied global strain of 3% to 4%, the lost DIC pixels measurement increases for both specimens. The difference between variations of lost DIC pixels measurements and hybrid method measurements in Fig. 12 before an applied global strain of 4% can thus be used to estimate the DIC tracking losses due to large deformation only. For the PTFE/epoxy specimen, the tracking area lost due to large deformation for a global strain inferior to 4% was thus calculated to be

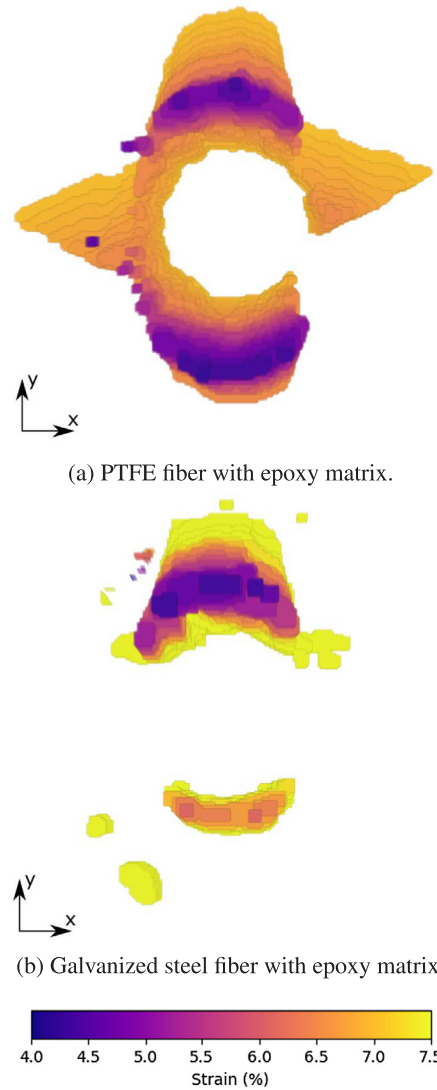


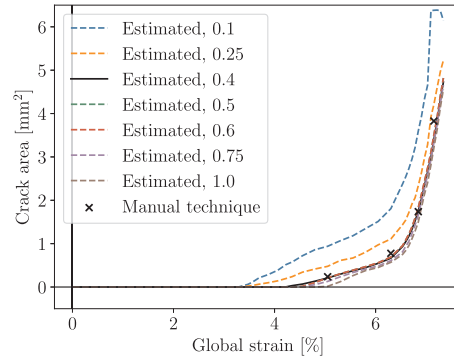
**Fig. 13.** Crack growth volume visualization. Extracted crack regions from each frame were stacked on top of each other in the direction perpendicular to the image. The color represents the strain in that frame. (For interpretation of the references to color in this figure legend, the reader is referred to the web version of this article.)

0.27 mm<sup>2</sup>, and 0.35 mm<sup>2</sup> for the galvanized steel/epoxy specimen.

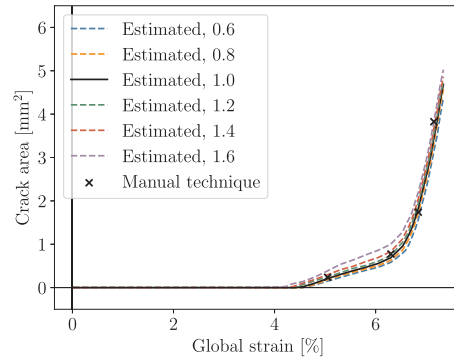
## 6.2. Crack path and bonding force

The computed crack paths for the PTFE/epoxy and galvanized steel/epoxy specimens are presented in Fig. 11. Fig. 11a shows that the crack path is transverse in the case of the PTFE fiber specimen. For the galvanized steel/epoxy specimen, it is also transverse but appears to be offset in the positive  $y$  direction. This difference is attributed to strong bonding between galvanized steel and epoxy. Strain measurements for the PTFE/epoxy and galvanized steel/epoxy specimens, provided in [43], show that the PTFE fiber is completely debonded at the free surface before specimen failure, while the galvanized steel/epoxy specimen remains bonded along the horizontal ( $x$ ) diameter of the fiber. Since the PTFE/epoxy specimen presents no bonding, specimen failure eventually occurs due Mode I cracks growing through the already debonded surface being pulled along the  $y$  direction. For the galvanized steel/epoxy specimen, a crack eventually appears between one of the bonded areas along the area around the  $x$  diameter, which remained bonded, and the top or bottom of the interfacial crack. Different fiber/matrix bonding strengths thus generate different crack paths in the reference frame. This result shows how this method can be used to estimate, qualitatively, the bonding strength between two different fiber/matrix couples.

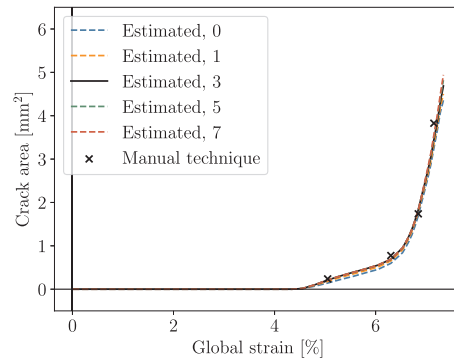




(a)



(b)



(c)

**Fig. 14.** Sensitivity of the crack area with respect to the proposed algorithm parameters. Results for the optimal parameter value are rendered as a solid line. The estimated crack area is also compared against the value measured manually. (a) Crack area estimation as a function of the entropy filter subset size. (b) Crack area estimation while varying the threshold value of the entropy image filter. (c) Crack area estimation while varying the number of dilations applied to the DIC-based crack area before using it in the hybrid method.

### 6.3. Parameter study

Fig. 14 shows our method's stability with respect to its parameters. The most impactful parameter is the entropy filter subset size, measured as a fraction of the DIC subset size. Larger sizes increase robustness, but lead to false-negatives, reducing the estimated crack area (Fig. 14a). In contrast, very small subset sizes result in false-positives, thus overestimating the crack area. Here we found that values ranging from 0.4 and 0.75 produced the most accurate results with respect to our manual measurements.

The second studied parameter is the threshold applied to the image entropy (Section 4.1.1). Smaller threshold values make stronger assumptions about the crack area's visual homogeneity, thus producing a more conservative estimate, and vice versa (Fig. 14b). The optimal threshold choice, as well as the subset size for the entropy filter, depend on the speckle pattern's quality: a

more coarse-grained pattern may require a larger subset size and a smaller threshold value to avoid classifying random imperfections as cracks. We found that a threshold value of 1 yielded accurate results.

The final parameter is the number of dilations applied to the DIC-based crack before using it as a search area for the hybrid method (Section 4.2.1). The value should be sufficiently large to include the whole crack before applying image filters to narrow the selection. Due to inaccuracy of the DIC-based crack, small values result in overly restricted search area, reducing the estimated crack area (Fig. 14c). Here values of three and above resulted in an accurate estimate.

Overall, the method appears to be fairly insensitive to the choice of parameters, with gradual changes to their values influencing the results in a regular and predictable way. Optimal parameter values can quickly be selected by performing several runs of our method and comparing the results to a crack area manual measurement for an arbitrary time-step.

#### 6.4. Limitations of the study

The subset size used during the DIC analysis is a parameter of the hybrid method. This limitation makes the method dependent of the subset size used during DIC, which might be unknown or not available. In addition, Fig. 14 shows that entropy filter subset size (which is obtained from the DIC subset size) is the most impactful parameter of the method.

This method does not help measuring displacements or computing strain fields at the edges of the crack. This method does not affect the DIC process nor it compensates for it where it struggles to compute fields. The hybrid method determines the crack area and path. However, this also means that, if the crack area and path are quantities of interest, they can be obtained out of any DIC software or code that provides the confidence value for each pixel of an image. The hybrid method can thus easily be used with commercial DIC software (which are local DIC based) that was employed for an experiment during which cracks appeared.

It was possible to estimate a crack area that is in agreement with manual measurements. It was also possible to determine a crack path in the reference frame of the camera which was presented in Fig. 11. Since the displacement and strain fields at the edges of a crack are unknown, due to limitations of the local DIC method, it is not possible to retrace back all pixels from a deformed image that contains a crack to their reference positions. Because of this local DIC limitation, it is not possible to validate the crack path in the reference coordinates through the DIC results. It is also not possible to determine the crack path in the reference frame as the material is completely deformed, making it impossible to determine the crack path in the initial, undamaged, configuration. The reference crack path presented in this work can thus be considered as an accurate estimate at best.

#### 7. Conclusion and outlook

We introduced a hybrid approach that relies on image processing techniques combined with digital image correlation for tracking and extracting crack surfaces. We validated our methods on crack areas manually measured. This observation suggests that the manual time consuming task for this procedure can be automated. Moreover, the hybrid approach is able to detect smaller crack areas that cannot be easily seen by eye, due to their size.

The crack surface mapping back to the initial configuration is valuable for two different communities. This information could be used by the computational engineering community to advance damage related simulations. This mapping could be used to indicate, for example, where to use cohesive elements to obtain more accurate benchmarks against experimental data. For the experimental mechanics community, this information could be used to gather more insights on how cracks grow and the corresponding crack paths. The volume-based rendering of time-dependent crack growth delivers a concise overview of crack growth. This representation can be used to quantitatively summarize the damage history of a specific fiber/matrix experiment. This representation could be extended to highlight the differences in crack initiation and crack growth between mechanisms in materials with different properties.

Quantitative measurements of interfacial crack growth rate are provided for each analyzed specimen. Results showed that fiber/matrix interfacial crack initiation under transverse load appears to be independent of fiber/matrix bonding strength and fiber mechanical properties. Interfacial crack growth rate and interfacial crack growth into the matrix are significantly delayed thanks to strong bonding.

This approach was tested on a simpler case with a single-fiber per specimen for which manual measurement would be, although time-consuming for all images, possible. Future works related to this method would be the analysis of experimental cases with a multitude of fibers and micro-cracks simultaneously growing, for which manual measurements would be too complex for an operator.

#### Appendix A. Supplementary material

Supplementary data associated with this article can be found, in the online version, at <https://doi.org/10.1016/j.engfracmech.2019.106485>.

#### References

- [1] Hild F, Roux S. Digital image correlation: from displacement measurement to identification of elastic properties - a review. *Strain* 2006;42(2):69–80.
- [2] Chevalier L, Calloch S, Hild F, Marco Y. Digital image correlation used to analyze the multiaxial behavior of rubber-like materials. *Eur J Mech A Solids* 2001;20(2):169–87.
- [3] Périé J-N, Calloch S, Cluzel C, Hild F. Analysis of a multiaxial test on a c/c composite by using digital image correlation and a damage model. *Exp Mech* 2002;42(3):318–28.
- [4] Mathieu F, Hild F, Roux S. Identification of a crack propagation law by digital image correlation. *Int J Fatigue* 2012;36(1):146–54.

- [5] Périé JN, Leclerc H, Roux S, Hild F. Digital image correlation and biaxial test on composite material for anisotropic damage law identification. *Int J Solids Struct* 2009;46(11–12):2388–96.
- [6] Hild F, Roux S. Digital image correlation: from displacement measurement to identification of elastic properties – a review. *Strain* 42(2):69–80. doi: <https://doi.org/10.1111/j.1475-1305.2006.00258.x>.
- [7] Pan B, Qian K, Xie H, Asundi A. Two-dimensional digital image correlation for in-plane displacement and strain measurement: a review. *Meas Sci Technol* 2009;20(6):062001.
- [8] Sutton MA, Orteu J-J, Schreier HW. *Image correlation for shape, motion and deformation measurements: basic concepts, theory and applications*. New York, N.Y.: Springer; 2009.
- [9] Wang B, Pan B. Subset-based local vs. finite element-based global digital image correlation: a comparison study. *Theor Appl Mech Lett* 2016;6(5):200–8. <https://doi.org/10.1016/j.taml.2016.08.003>.
- [10] Mortazavi F, Lévesque M, Villemure I. Image-based continuous displacement measurements using an improved spectral approach. *Strain* 2013;49(3):233–48. <https://doi.org/10.1111/str.12031>.
- [11] Rethore J, Hild F, Roux S. Shear-band capturing using a multiscale extended digital image correlation technique. *Comput Methods Appl Mech Eng* 2007;196(49–52):5016–30.
- [12] Hild F, Roux S. Comparison of local and global approaches to digital image correlation. *Exp Mech* 2012;52(9):1503–19. <https://doi.org/10.1007/s11340-012-9603-7>.
- [13] Sutton M, Wolters W, Peters W, Ranson W, McNeill S. Determination of displacements using an improved digital correlation method. *Image Vis Comput* 1983;1(3):133–9.
- [14] Mehdikhani M, Aravand M, Sabuncuoglu B, Callens MG, Lomov SV, Gorbatiikh L. Full-field strain measurements at the micro-scale in fiber-reinforced composites using digital image correlation. *Compos Struct* 2016;140:192–201.
- [15] Correlated S. Vic-3D Help Manual, Correlated Solutions; 2010. URL <http://www.correlatedsolutions.com/installs/Vic-3D-2010-manual.pdf>.
- [16] Sakanashi Y, Gungor S, Forsey A, Bouchard P. Measurement of creep deformation across welds in 316H stainless steel using digital image correlation. *Exp Mech* 2017;57(2):231–44. <https://doi.org/10.1007/s11340-016-0245-z>. <http://link.springer.com/10.1007/s11340-016-0245-z>.
- [17] Seon G, Makeev A, Cline J, Armanios E. Assessing 3d mechanical properties of composites based on digital image correlation; 2015.
- [18] Croom B, Wang W-M, Li J, Li X. Unveiling 3d deformations in polymer composites by coupled micro X-ray computed tomography and volumetric digital image correlation. *Exp Mech* 2016;56(6):999–1016. <https://doi.org/10.1007/s11340-016-0140-7>.
- [19] Triconnet K, Derrien K, Hild F, Baptiste D. Parameter choice for optimized digital image correlation. *Opt Lasers Eng* 2009;47(6):728–37. <https://doi.org/10.1016/j.optlaseng.2008.10.015> <https://linkinghub.elsevier.com/retrieve/pii/S0143816609000165>.
- [20] Carroll J, Efstathiou C, Lambros J, Sehitoğlu H, Hauber B, Spottswood S, et al. Investigation of fatigue crack closure using multiscale image correlation experiments. *Eng Fract Mech* 2009;76(15):2384–98. <https://doi.org/10.1016/j.engfractmech.2009.08.002> <https://linkinghub.elsevier.com/retrieve/pii/S0013794409002501>.
- [21] Rannou J, Limodin N, Réthoré J, Gravouil A, Ludwig W, Baïetto-Dubourg M-C, et al. Three dimensional experimental and numerical multiscale analysis of a fatigue crack. *Comput Methods Appl Mech Eng* 2010;199(21–22):1307–25. <https://doi.org/10.1016/j.cma.2009.09.013> <https://linkinghub.elsevier.com/retrieve/pii/S0045782509003119>.
- [22] Casperson MC, Carroll JD, Lambros J, Sehitoğlu H, Dodds RH. Investigation of thermal effects on fatigue crack closure using multiscale digital image correlation experiments. *Int J Fatigue* 2014;61:10–20. <https://doi.org/10.1016/j.ijfatigue.2013.11.020> <https://linkinghub.elsevier.com/retrieve/pii/S0142112313003356>.
- [23] Helm JD. Digital image correlation for specimens with multiple growing cracks. *Exp Mech* 2008;48(6):753–62. <https://doi.org/10.1007/s11340-007-9120-2>.
- [24] Mohan A, Poobal S. Crack detection using image processing: a critical review and analysis. *Alexandria Eng J* doi: <https://doi.org/10.1016/j.aej.2017.01.020>.
- [25] Yamaguchi T, Hashimoto S. Fast crack detection method for large-size concrete surface images using percolation-based image processing. *Mach Vis Appl* 2010;21(5):797–809.
- [26] Yamaguchi T, Nakamura S, Hashimoto S. An efficient crack detection method using percolation-based image processing. *Industrial electronics and applications, 2008. ICIEA 2008. 3rd IEEE conference on. IEEE; 2008. p. 1875–80*.
- [27] Iliopoulos S, Aggelis DG, Pyl L, Vantomme J, Van Marcke P, Coppens E, et al. Detection and evaluation of cracks in the concrete buffer of the Belgian Nuclear Waste container using combined NDT techniques. *Constr Build Mater* 2015;78(Supplement C):369–78. <https://doi.org/10.1016/j.conbuildmat.2014.12.036>.
- [28] Hamrat M, Boulekbache B, Chemrouk M, Amziane S. Flexural cracking behavior of normal strength, high strength and high strength fiber concrete beams, using Digital Image Correlation technique. *Constr Build Mater* 2016;106(Supplement C):678–92. <https://doi.org/10.1016/j.conbuildmat.2015.12.166>.
- [29] Alam SY, Loukili A, Grondin F, Rozière E. Use of the digital image correlation and acoustic emission technique to study the effect of structural size on cracking of reinforced concrete. *Eng Fract Mech* 2015;143(Supplement C):17–31. <https://doi.org/10.1016/j.engfractmech.2015.06.038>.
- [30] Doitrand A, Fagiano C, Hild F, Chiaruttini V, Mavel A, Hirsekorn M. Mesoscale analysis of damage growth in woven composites. *Compos Part A: Appl Sci Manuf* 2017;96:77–88. <https://doi.org/10.1016/j.compositesa.2017.02.018> <https://linkinghub.elsevier.com/retrieve/pii/S1359835X17300660>.
- [31] Réthoré J, Hild F, Roux S. Extended digital image correlation with crack shape optimization. *Int J Numer Meth Eng* 2008;73(2):248–72.
- [32] Besnard G, Hild F, Roux S. “Finite-Element” displacement fields analysis from digital images: application to Portevin–Le Châtelier bands. *Exp Mech* 2006;46(6):789–803. <https://doi.org/10.1007/s11340-006-9824-8>.
- [33] Pan B, Wang B, Lubineau G. Comparison of subset-based local and FE-based global digital image correlation: theoretical error analysis and validation. *Opt Lasers Eng* 2016;82:148–58. <https://doi.org/10.1016/j.optlaseng.2016.02.019> <https://linkinghub.elsevier.com/retrieve/pii/S0143816616000579>.
- [34] Blom J, Wastiels J, Aggelis DG. Application of acoustic emission on the characterization of fracture in textile reinforced cement laminates. *Sci World J* 2014;2014:e178020. <https://doi.org/10.1155/2014/178020> <http://www.hindawi.com/journals/tswj/2014/178020/abs/>.
- [35] Touni RB, Renard J, Monin M, Nimdum P. Fatigue damage modelling of continuous E-glass fibre/epoxy composite. *Procedia Eng* 2013;66:723–36. <https://doi.org/10.1016/j.proeng.2013.12.126> <http://www.sciencedirect.com/science/article/pii/S1877705813019590>.
- [36] Talreja R, Veer Singh C. *Damage and failure of composite materials*. Cambridge university press ed. Cambridge University Press; 2012.
- [37] Hinton MJ, Kaddour AS, Soden PD. The world-wide failure exercise: Its origin, concept and content. In: Hinton MJ, Kaddour AS, Soden PD, editors. *Failure criteria in fibre-reinforced-polymer composites* Oxford: Elsevier; 2004. p. 2–28. <https://doi.org/10.1016/B978-008044475-8/50002-0> [chapter 1.1].
- [38] Kaddour A, Hinton M. Maturity of 3d failure criteria for fibre-reinforced composites: comparison between theories and experiments: Part B of WWFE-II. *J Compos Mater* 2013;47(6–7):925–66. <https://doi.org/10.1177/0021998313478710>.
- [39] Martyniuk K, Sørensen BF, Modregger P, Lauridsen EM. 3d in situ observations of glass fibre/matrix interfacial debonding. *Compos Part A: Appl Sci Manuf* 2013;55:63–73.
- [40] Sørensen BF, Goutianos S. Mixed Mode cohesive law with interface dilatation. *Mech Mater* 2014;70:76–93.
- [41] Vernerey FJ, Kabiri M. Adaptive concurrent multiscale model for fracture and crack propagation in heterogeneous media. *Comput Methods Appl Mech Eng* 2014;276:566–88.
- [42] Richefeu V, Chrysochoos A, Huon V, Monerie Y, Peyroux R, Wattrisse B. Toward local identification of cohesive zone models using digital image correlation. *Eur J Mech A Solids* 2012;34:38–51. <https://doi.org/10.1016/j.euromechsol.2011.12.001> <http://www.sciencedirect.com/science/article/pii/S0997753811001690>.
- [43] Tabiai I, Delorme R, Theriault D, Lévesque M. In-situ full field measurements during inter-facial debonding in single fiber composite under transverse load. *Exp Mech* doi: <https://doi.org/10.1007/s11340-018-0429-9>. <http://link.springer.com/10.1007/s11340-018-0429-9>.
- [44] Tabiai Ilyass, Delorme Roland, Theriault Daniel, Lévesque Martin. Additional data for the In-situ full field measurement during inter-facial debonding in single fiber composite under transverse load, type: dataset (Feb. 2018). doi: <https://doi.org/10.5281/zenodo.1188272>.
- [45] Biswas SK, Vijayan K. Friction and wear of PTFE – a review. *Wear* 1992;158(1):193–211. [https://doi.org/10.1016/0043-1648\(92\)90039-B](https://doi.org/10.1016/0043-1648(92)90039-B).
- [46] Plummer J. What makes epoxy resins good adhesives? Why do they bond so strongly to surfaces? Tech. rep. Londonderry, NH 03053: Mereco Technologies; 2014.
- [47] Nakazawa M. Mechanism of adhesion of epoxy resin to steel surface. *Nippon Steel Technical Report* 63 (63); 2014. p. 16–22. URL <http://www.nssmc.com/en/>

- [tech/report/nsc/pdf/6303.pdf](#).
- [48] Munse WH. HIGH-STRENGTH BOLTING. <https://trid.trb.org/view/102941>.
  - [49] Sutton M, Yan J, Tiwari V, Schreier H, Orteu J. The effect of out-of-plane motion on 2d and 3d digital image correlation measurements. *Opt Lasers Eng* 2008;46(10):746–57. <https://doi.org/10.1016/j.optlaseng.2008.05.005><http://linkinghub.elsevier.com/retrieve/pii/S0143816608000985>.
  - [50] Byrne Elisha, Simonsen Micah. Resolution and accuracy - Knowledge base; Oct. 2016. URL <http://www.correlatedsolutions.com/support/index.php?Knowledgebase/Article/View/8/1/resolution-and-accuracy>.
  - [51] Serra J. *Image analysis and mathematical morphology*. Orlando, FL, USA: Academic Press, Inc.; 1983.
  - [52] Zhang TY, Suen CY. A fast parallel algorithm for thinning digital patterns. *Commun ACM* 1984;27(3):236–9. <https://doi.org/10.1145/357994.358023>.
  - [53] Russ JC. *The image processing handbook*. 6th ed. Boca Raton, FL, USA: CRC Press, Inc; 2011.
  - [54] Shannon CE. A mathematical theory of communication. *Bell Syst Tech J* 1948;27(3):379–423.
  - [55] Jones E, Oliphant T, Peterson P, et al. SciPy: open source scientific tools for Python; 2001. <http://www.scipy.org/>.
  - [56] van der Walt S, Schönberger JL, Nunez-Iglesias J, Boulogne F, Warner JD, Yager N, et al. The scikit-image contributors, scikit-image: image processing in Python. *PeerJ* 2014;2:e453. <https://doi.org/10.7717/peerj.453>.